6
Mapping Spatio-Temporal Electrophysiological Activity in Hippocampal Slices with Conformal Planar Multi-Electrode Arrays

Walid Soussou, Ghassan Gholmieh, Martin Han, Ashish Ahuja, Dong Song, Min-Chi Hsiao, Zhuo Wang, Armand R. Tanguay Jr., and Theodore W. Berger

6.1 Introduction

Over the last two decades, technological advances in the fields of microchip and electronics manufacturing have enabled an increase in the production and use of silicon-based multi-electrode arrays. (Singer, 2000; Morin et al., 2005) These multi-electrode arrays or MEA for short, have come in a variety of shapes and materials, but fall into two broad classes: thin and sharp (implantable) or dish-based (planar). Although many investigations are currently undertaking research in vivo with implantable versions, this chapter focuses on applications of planar MEAs (pMEA), which are very well suited for in vitro experiments with slice or dissociated cells preparations. This chapter illustrates the utility and advantages of pMEAs in electrophysiological investigations with acute hippocampal slices, while introducing a new generation of conformally designed higher-density pMEAs as an adjuvant approach to facilitate and enhance MEA-based research.

Currently, the research being undertaken on pMEAs ranges from studying processes of neuronal plasticity underlying learning and memory, to tracking activity development in networks, and also pharmacological drug screening and testing. These diverse applications can be classified, based on the intricacy of their methodology, into the following nonmutually exclusive categories: (1) MEAs can be used as a multitude of single independent electrodes for rapid high-throughput experiments; (2) the spatial relations between electrode tips can be used synergistically to map electrical activity to tissue location; (3) recording simultaneously from multiple electrodes allows correlation of temporal information, which is not possible with many recordings from single electrodes; (4) the combination of spatial and temporal monitoring reveals the spatiotemporal dynamics of the neuronal network; (5) the ability to maintain cultured preparations on pMEAs allows long-term physiological investigations; and (6) recording and stimulating through the pMEA creates two-way communication with the tissue that is indispensable for investigating and developing neuroprosthetic applications.

High-throughput applications involve sampling several electrodes out of the total number on the MEA and selecting a representative one, or treating subgroups statistically as multiple samples from a homogeneous population. Electrodes within a particular cytoarchitectural region of a slice usually record similar neural responses. This redundancy of observed signals can be used to enhance the statistical significance of results by grouping responses into larger sample sizes. Similar time savings are achieved in cell cultures, where the multitude of electrodes records the activity of numerous cells at the same time, thereby decreasing the number of individual experiments needed to reach a significant population sample. Such high-throughput use of MEAs as biosensors has been applied to drug screening using cell culture (Pine, 1980; Gross et al., 1995) and hippocampal slice rhythmic activity (Shimono et al., 2000). In the first case, drugs are classified according to changes in the firing activity of neuronal cells cultured on MEAs (Gross et al., 1995, 1999). In the second case, changes in the frequency of carbachol-induced theta rhythmic oscillations in hippocampal slices are correlated with specific drug properties (Shimono et al., 2000). In both cases, the MEAs provided multiple sample points in different regions of the network, which enabled either a quick selection of an optimal site or averaging several channels for greater statistical accuracy.

In contrast to using array electrodes as individual and independent streams of data, the spatial arrangement of electrodes can be used to generate spatial maps of the activity in a slice. Any parameter of the recorded potentials can be plotted in a color-coded matrix according to the relative spatial positions of the electrodes in order to generate topographic activity maps. Such spatial activity maps can be matched to a picture of the slice showing the actual electrode positions in order to visualize the activity in relation to the subregions of a slice (Shimono et al., 2000) or map the spatial extent of a response along a network (Jimbo and Robinson, 2000). In addition, if electrodes are close enough to each other, they enable current source density (CSD) analysis, which can elucidate the origins and meaning of the complex field potentials recorded (Wheeler and Novak, 1986).

The ability to simultaneously record from all the MEA electrodes over time enables correlation of activity between different parts of a network in order to study their patterns and plasticity in cell and tissue preparations. The temporal sequence of firing of ensembles of cells can provide information on network states. Beggs and Plenz (2003) analyzed cell bursting avalanches to describe the stability of the network. Jimbo et al. (1999) reported on time-dependent synaptic plasticity in networks of cultured cells in observing that connections between cells that fired within 20 msec before the other were potentiated after tetanus, whereas connections between cells negatively correlated within 20 msec were depressed.

pMEAs combine spatial and temporal information and enable the conversion of static spatial activity maps into dynamic spatiotemporal map sequences. These series of maps can be joined as frames of a movie to visually trace the propagation of spontaneous, evoked, or rhythmic activity across the slice. For example, Novak and Wheeler (1989) studied the temporal propagation of seizure activity, and Shimono et al. (2000) localized and spatiotemporally followed the origin of theta rhythm

generated by carbachol in a slice, both using CSD analysis of the signals recorded from the MEA.

The surface of pMEAs is ideal for long-term tissue cultures of both slices and dissociated cells, as it provides a flat, biocompatible, and sterilizable support with embedded electrodes that can continuously monitor culture activity without disrupting the closed system. Longer-term experiments can track changes in activity and plasticity of developing cultures and networks (Gross and Schwalm, 1994; Stoppini et al., 1997; Thiebaud et al., 1997; Jahnsen et al., 1999) under different chronic pharmacological treatments (Shimono et al., 2002).

Although several neuroprosthetics, such as cochlear, cortical (Chapin et al., 1999), and retinal (Humayun et al., 2003) devices rely on implantable in vivo MEA technology, pMEAs still play a major role in understanding network connectivity and dynamics (Meister et al., 1994; Warland et al., 1997). pMEAs are being used as an in vitro testing platform to first characterize the information processing of the target neuronal network, before undertaking in vivo experiments. In our current goal to replace the CA3 hippocampal area with a microchip (FPGA/VLSI) implementation of a nonlinear model of CA3 (Berger et al., 2001), we are using pMEAs to provide a functional proof-of-principle. pMEA experiments allow us first to generate nonlinear models, then to test hardware implementations in order to change parameters and conditions rapidly, cost effectively, and with fewer animals. Similarly, the retinal prosthesis project relies on understanding underlying network dynamics and plasticity of the retina in order to transform incident light into an electrical stimulation pattern that will produce correct visual percepts (Humayun and Weiland, personal communications). Retinal stimulation and recording experiments are thus currently being undertaken on pMEAs to develop a nonlinear mathematical model of the retinal network that will be implemented in the next generation of retinal prostheses (Chichilnisky and Kalmar, 2003; Frechette et al., 2005).

6.2 High-Density Conformal pMEAs

The above-mentioned applications of pMEAs illustrate their versatility and advantages of having multiple electrodes over a single electrode. These advantages could be augmented by increasing the number of electrodes, that is, by increasing the number of sampling points and spatial resolution. Unfortunately, physical as well as technological constraints limit the number of possible electrodes on an MEA. The first obstacle is overcrowding of electrode leads, which can produce unwanted noise and crosstalk between closely spaced lines, and require more complex manufacturing solutions, such as lead stacking or electrode addressing. The second impediment involves connectors, which are difficult to keep small and reliable. The third barrier is the size and cost of signal modulation, digitization, and storage hardware. That is, of course, without mentioning the increased complexity and time consumption of data analysis. This limit on the number of electrodes creates a tradeoff in array design: electrodes can either sparsely

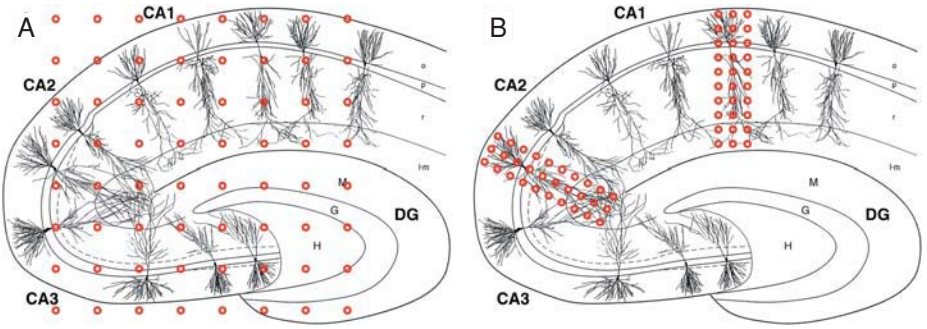

FIGURE 6.1. Electrode positions matched to a drawing of a hippocampal slice with representative cell bodies, axons, and dendrites traced from Nissl stains (Ishizuka et al., 1995). (A) A square 8 × 8 array of electrodes is overlaid on the slice drawing. (B) Two high-density 3 ×10 rectangular arrays whose angles and separation conform to the cytoarchitecture of the slice are overlaid on the CA2 and CA1 pyramidal cells. (Electrode size and spacing not to scale.0

cover a large surface area or be closely spaced (high-density) over a smaller one. Figure 6.1 illustrates the tradeoff due to the constraint on electrode number with two arrangements of electrodes overlaid on a drawing of a hippocampal slice. A low-density square matrix 8 × 8 array (Figure 6.1A) can record field potentials from several different areas of the slice while providing only two and rarely three electrodes along the orientation of a particular cell group. The two more densely packed 3 × 10 subarrays (Figure 6.1B) cover only two pyramidal populations (one in CA1 and another in CA2), but match the correct orientation of the cells' dendritic axis, which allows CSD analysis and multiple points for bipolar stimulation (see below).

This tradeoff has led us to create and test several new high-density conformal pMEAs that are custom designed for our experimental purposes. These pMEAs have several high-density clusters of electrodes whose orientation and location conform to the cytoarchitecture of the slice. The hippocampal slice is an ideal tissue preparation for pMEAs, as its intrinsic two-dimensional trisynaptic excitatory cascade network from dentate gyrus to CA3 and CA1 subregions (DG → CA3 → CA1) is preserved when the hippocampus is sliced along its longitudinal axis. (Andersen et al., 1971) The following experimental examples are designed to illustrate the above-listed applications of pMEAs in electrophysiological experiments on acute hippocampal slices, while emphasizing the advantages of our new conformal high-density designs.

6.2.1 High-Throughput Multiple Independent Sites

We have used pMEAs to build a hippocampal-based biosensor for rapid neurotoxins detection (Gholmieh et al., 2001, 2003). The detection of the chemical compounds is based on a novel quantification method for analyzing short-term

plasticity (STP) of the CA1 system in acute hippocampal slices, using random electrical impulse sequences as inputs and population spike (PS) amplitudes as outputs. STP is quantified by the first- and the second-order Volterra kernels using a variant of the Volterra modeling approach. Since they describe the functional state of the biosensor, the Volterra kernels changed differently depending on the chemical compounds that were added to the slice medium, which enabled its classification.

Determining the location of the optimal CA1 population spike response is a critical parameter for this approach. Using 8 × 8 pMEAs with an interelectrode distance of 150 μm from the University of North Texas (CNNS, Denton, TX, USA), extracellular potentials in the CA1 region were recorded from rat hippocampal slices. All the slices described below were from male Sprague–Dawley rats that were anaesthetized before decapitation. The hippocampi were dissected under cold artificial cerebrospinal fluid (aCSF (in mM): NaCl, 128; KCl, 2.5; NaH_2PO_4, 1.25; $NaHCO_3$, 26; Glucose, 10; $MgSO_4$, 2; ascorbic acid, 2; $CaCl_2$, 2, aerated with a mixture of 95% O_2 and 5% CO_2), and sectioned into 400 μm slices. The tissue was then allowed to rest for at least one hour at room temperature before positioning on the pMEAs and starting the experiments under continuous perfusion of aCSF with reduced $MgSO_4$ (1 mM). Figure 6.2 shows a paired-pulse experiment with a hippocampal slice positioned over the array (A) and potentials recorded at a subset of electrodes of the array (B). In these experiments, slices were stimulated using external bipolar nichrome electrodes, which allow larger current injections than array electrodes. The corresponding 16 recordings spanned *stratum oriens*, *stratum pyramidale*, and the apical dendritic region (*stratum moleculare* and *stratum radiatum*). The optimal recording for our purposes was the one that showed the largest amplitude with a well-defined population spike overriding a positive excitatory postsynaptic potential (EPSP). Once the specific electrode with the corresponding channel was chosen, a random train was delivered to the slice. On several occasions, however, we have been faced with the inability to obtain signals that fit the above criteria due to the scarcity of electrodes and nonoptimal stimulation position.

Faced with the limitations of the currently available pMEAs, we have designed a new pMEA that would optimize CA1 input (stimulation)–output (recording) properties. This pMEA has a 2 × 8 subarray to stimulate the Schaffer collaterals fibers which constitute the major excitatory inputs to CA1 pyramidal cells, and a 4 × 12 subarray to record the output of these cells (Figure 6.3A). This novel pMEA, designed to match CA1's cytoarchitecture, eliminates the need to reposition the slice or stimulation electrode for optimizing stimulation and recording locations. The following paragraph describes this optimization protocol.

Hippocampal slices were positioned over the array with the 2 × 8 subarray under the Schaffer collateral pathway, and the 4 × 12 subarray under CA1 pyramidal cells (Figure 6.3A). One column of the 2 × 8 subarray was chosen for stimulation (S column, Figure 6.3B). The eight electrodes in the stimulation column formed seven possible adjacent pair combinations: that is, S1–2, S2–3, . . . , S7–8. A testing paired-pulse stimulation (30 msec interval) of 70 to 100 μA was

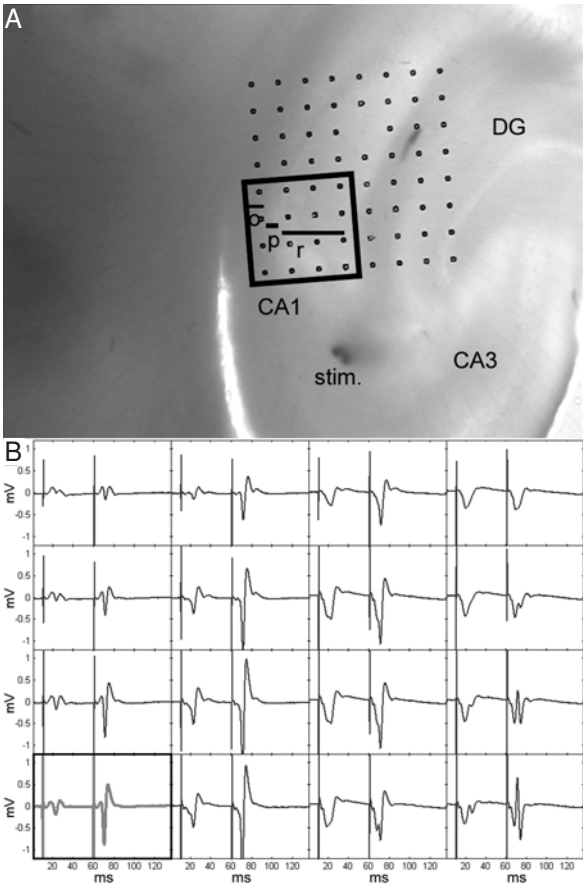

FIGURE 6.2. Recording hippocampal slice evoked responses with a pMEA. (A) Hippocampal slice positioned over the 8 × 8 array. (B) The corresponding recording from a 4 × 4 subset. The corresponding 16 recordings span *stratum oriens* (o), the cell body layer and the apical dentritic region (*stratum moleculare* (m), and *stratum radiatum* (r)). The optimal recording for our purposes was the one (highlighted in the lower left quadrant) that showed the largest amplitude with a well-defined population spike overriding a positive excitatory postsynaptic potential (EPSP).

delivered sequentially through each pair to identify the pair that yielded the largest amplitude population spike. That stimulation pair was then used to generate an input/output (I/O) curve, by incrementally increasing the stimulation intensity over a 10 to 250 μA range. The stimulation intensity was then set to yield the half-maximal response, and five sets of paired pulses were delivered again through each of the seven electrode pairs and then the responses were averaged. One column of the 4 × 12 subarray was used for recording (R column, Figure 6.3B). In this particular experiment, the laminar profile recorded in the R column shows a

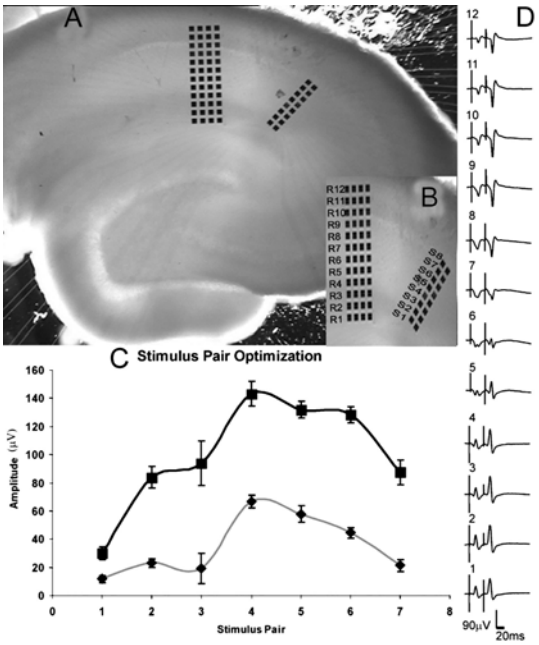

FIGURE 6.3. Optimization of the input–output properties of Schaffer collaterals–CA1: (A) hippocampal slice on a pMEA; (B) blow-up of the recording (R) and stimulation sites (S); (C) population spike amplitude responses for the first (gray) and the second pulses (black) recorded at R11, plotted against the stimulation pair number; (D) laminar profile of FP recordings.

clear pyramidal population spike at R8–12 and the largest dendritic component at R3 and R4 (Figure 6.3D). The recording electrode R11 had the largest discernable population spike. Its stimulation optimization graph is shown in Figure 6.3C where the population spike amplitude is plotted against the different possible stimulation pair combinations. The maximal response for this slice was thus obtained at R11 in response to stimulation from pair S5–S6. Hence, this array allowed us to rapidly localize an afferent pathway, and to optimize the stimulation location to obtain the largest response in the target area.

We were further interested in selectively stimulating two adjacent afferent pathways to dentate gyrus (DG), in order to compare interactions of their responses in the same slice. For this purpose, we designed the perforant path (PP)-DG-CA3 pMEA, which has three high-density subarrays: two 3×7 arrays that span the blades of the DG and one 3×6 array to record their mossy fiber/CA3 outputs. The PP is the major excitatory projection into DG and consists of two anatomically and functionally discrete subdivisions, medial and lateral PP. The lateral PP originates in the ventrolateral entorhinal cortex, and terminates in the outer third of the DG molecular layer, whereas the medial PP originates in the dorsomedial entorhinal cortex, and synapses in the middle third of the DG molecular layer (Steward,

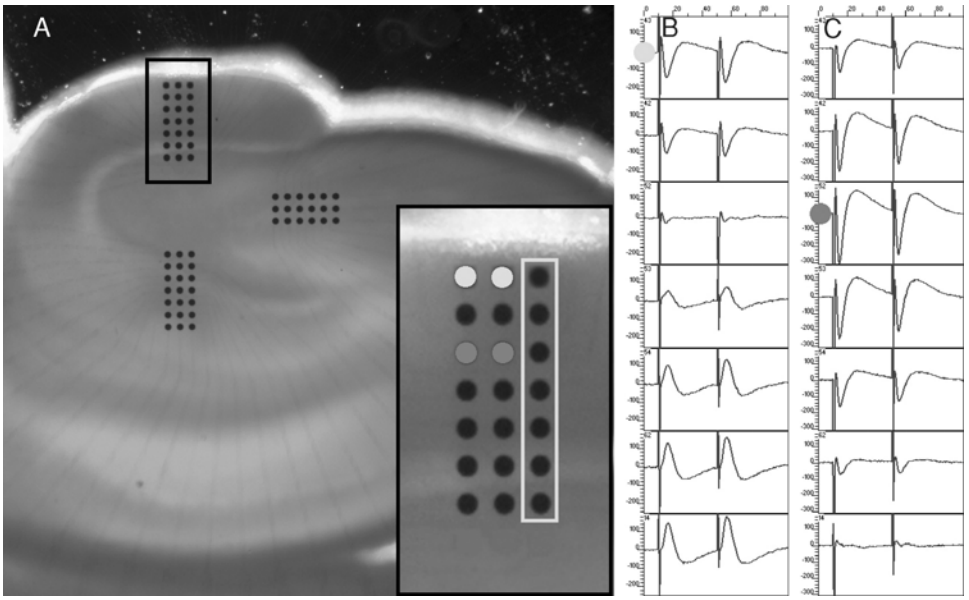

FIGURE 6.4. Paired-pulse facilitation and depression in dentate gyrus: (A) photomicrograph of dentate on a three subarray pMEA. The electrodes highlighted in light and dark gray correspond, respectively, to lateral and medial perforant path stimulation sites, and the white box marks the electrodes whose responses are graphed in B and C; (B) response of a column of electrodes to bipolar paired-pulse stimulation at the light electrodes in lateral PP; (C) paired-pulse depression in response to medial PP stimulation. (B),(C). The interstimulus interval was 50 msec. *Y*-axis: −250 to 250 μV, *X*-axis: 100 msec.

1976). Experimentally, the two pathways are distinguished by their anatomical location, and their responses to paired-pulse (pp) stimulation, whereby lateral PP shows facilitation and medial PP responses exhibit depression (McNaughton and Miller, 1984; Dahl et al., 1990). Each of these subpathways encompasses approximately 100 μm, and the electrodes are spaced 50 μm apart, therefore, by sequentially stimulating along a column, each subpathway is activated from at least two rows. We manufactured these pMEAs to fit into the Multi Channel Systems recording setup (MCS, Reutlingen, Germany; Gholmieh G. et al., 2005). The degree of selectivity of a pathway can then be determined by the amount of facilitation or depression observed.

Figure 6.4 shows an example distinguishing between medial and lateral PP in a rat hippocampal slice. After positioning the slice on the array, we sent bipolar stimulations through adjacent electrode pairs in rows, and recorded the responses along the third column. The electrodes highlighted in light gray were used to stimulate the outer third of the PP (B), which corresponds to lateral PP. A 50 msec interval pp produced an increase in the amplitude of the second evoked postsynaptic potential (PSP) compared to the first, hence exhibiting pp facilitation. In

contrast, stimulating the same slice through electrodes at medial PP (C, marked in dark gray) revealed pp depression at the same 50 msec interval. The facilitation and depression observed respectively at the anatomical lateral and medial pathways confirm that the two subpathways were indeed selectively excited. Paired-pulse stimulations at the electrodes in between the light and dark gray ones did not produce changes in PSP amplitudes, suggesting that both pathways might be partially stimulated, and canceled each other's effects. This experiment illustrates the ease with which this conformal pMEA, with its closely spaced electrodes was able to selectively activate two adjacent pathways. Such subpathway segregation is extremely difficult to achieve in the same slice with more widely spaced MEAs or inserted twisted-wire stimulating electrodes.

6.2.2 Spatial Mapping of Electrical Activity

In a heterogeneous tissue such as the hippocampal slice, which has several regions populated by different cell types with different interconnectivities, all the electrodes of a pMEA do not record the same signals. The spatial distribution of electrodes determines the subregions that are sampled, which may respond differently to different stimuli. The uniqueness of information carried by each electrode therefore reflects underlying slice cytoarchitecture, and provides information on functional physiology of various subregions. By arranging all electrode responses according to the pMEA topography, we obtain a spatial map of responses. The waveforms in Figures 6.2 through 6.4 are arranged according to their respective positions on the pMEA, and illustrate how responses vary over the slice. In Figure 6.2, the population spike amplitude varies in relation to the distance from the pyramidal cell layer. In Figure 6.4B, a reversal from a negative going potential to a positive one is observed, which indicates good isolation of afferent inputs. These spatial maps show the entire response at every electrode, and although they are comprehensive, visually extracting information from these formats may be hard. Another approach to display spatial maps is to extract the parameter of interest, transform its value into a color code, and then plot it according to its electrode position. By interpolating between adjacent electrode values, a color map is generated, which easily visualizes the topographic distribution of the parameter.

Figure 6.5 illustrates how useful and easy a color spatial map can be for visually presenting a long-term potentiation (LTP) experiment run on a 60 electrode pMEA. In LTP experiments, the amplitude of excitatory postsynaptic potentials (EPSP) is compared before and after high-frequency stimulation (HFS). The EPSP amplitude is therefore extracted and converted into a pseudo-color map that is overlaid on top of a picture of the experimental slice. The spread of the EPSP response is thus quickly visualized as the red area, and the post-HFS (Figure 6.5B) response is notably darker than the pre-HFS, thereby indicating potentiation. The ratio of post-HFS amplitude over pre-HFS amplitude is calculated to determine the percentage of LTP at each electrode. This percentage is color-coded and mapped in Figure 6.5D, which reveals in red the extent of CA1 that exhibited potentiation.

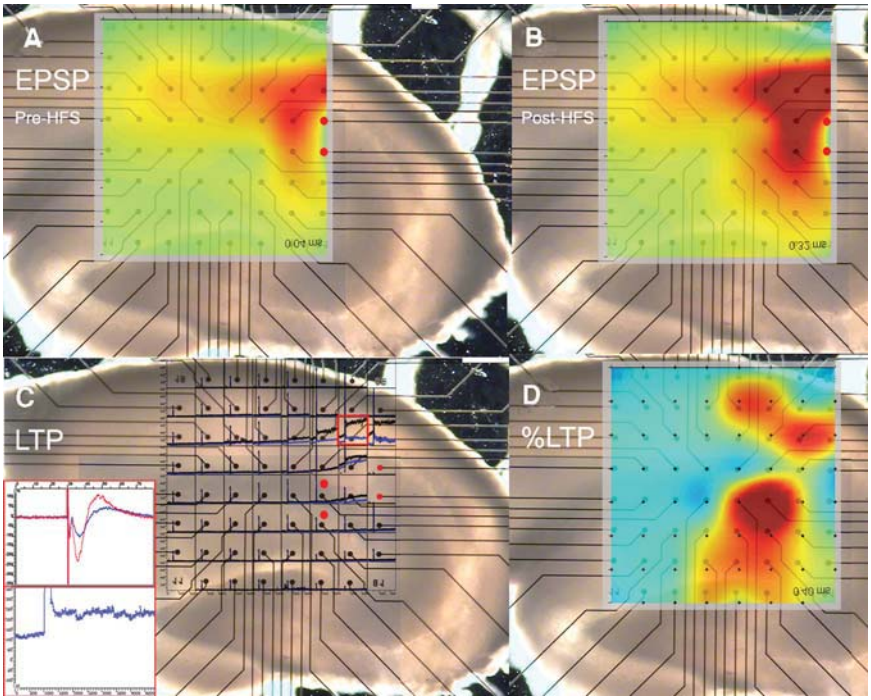

FIGURE 6.5. Extent of LTP is different than extent of response: (A) EPSP map showing CA1 response to Shaffer stimulation (color map reflects interpolation between EPSP amplitudes at recording electrodes, where red indicates 50 mV, dark blue −50 mV, and green 0 mV). (B) Same as in (A) only mapping the response after HFS potentiation. (C) Timecourse of LTP experiment plotting amplitude over time at each electrode location. Top inset shows overlay of EPSP waveforms pre- and post-HFS for the electrode boxed in red. Bottom inset shows that electrode's timecourse (box sizes 500 μV and 80 msec). (D) Spatial map showing extent of spread of potentiation (color map represents interpolation between percent change in amplitude at the recording electrodes between pre- and post-HFS, where red indicates 300%, and dark blue 0%).

This spatial map of LTP is a lot simpler to read than Figure 6.5C, which shows the time course of the LTP experiment at each electrode (we discuss spatiotemporal maps in the next section). It is interesting to observe that not all areas that showed an EPSP in Figures 6.5A and B were actually potentiated in C, and vice-versa.

The above spatial maps give an excellent picture of what is happening over the entire slice during the experiment; however, they do not provide information about the exact location of activity. There are not enough sampling points to produce accurate information about the differences along the dendritic tree of pyramidal cells. This low spatial resolution is further complicated by the fact that field potentials intermix in the tissue, and their sources may be missed between electrodes. High-density pMEAs sample more points per unit area, and enable

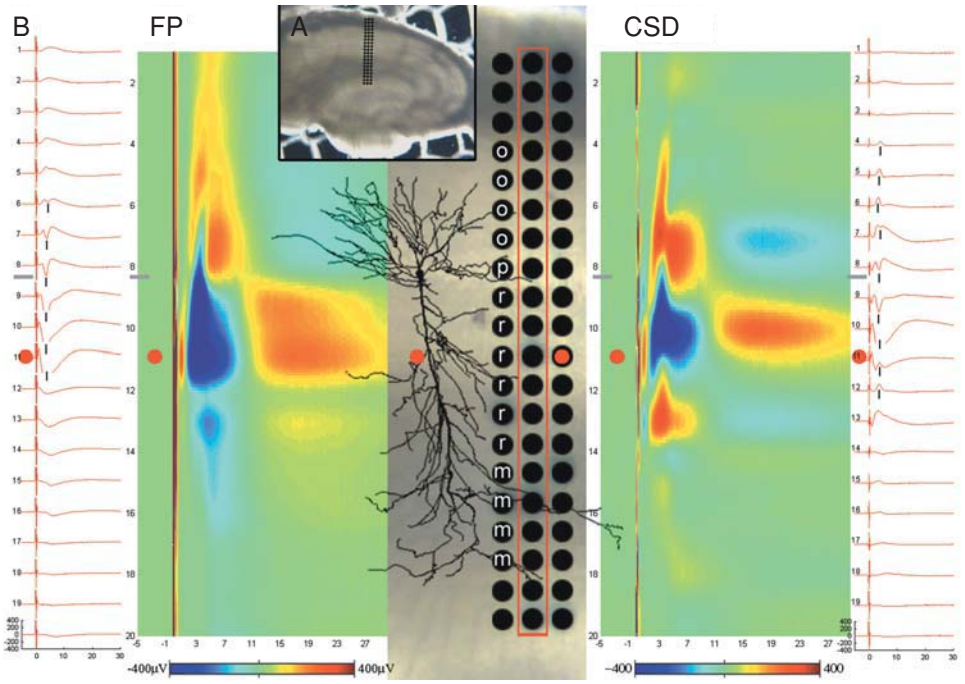

FIGURE 6.6. FP versus CSD in CA1: (A) photomicrograph of a hippocampal slice on the 20 × 3 pMEA; (B) CA1 laminar profile of the slice in (A) in response to stimulation at the electrode marked in red. The red traces show the recorded FP or the calculated CSD at the middle column (red box), with the numbers corresponding to the electrode position starting from the top. The color map shows the same values converted to a color scale and interpolated between electrodes. The trace drawing of a cell illustrates the relative position of the electrodes with respect to the CA1 pyramidal cells. The horizontal gray bars mark the cell layer. The vertical black lines mark the population spike. The stimulation occurred 10 msec after the beginning of the recording. (*x*-axis 35 msec, *y*-axis or color range −400 to +400 μV or CSD units. *Strata* are labeled in the electrodes: *oriens* (o), *pyramidale* (p), *radiatum* (r), and *moleculare* (m).)

CSD analysis. (Nicholson and Freeman, 1975; Miyakawa and Kato, 1986) The latter is a spatial filter that reveals sources and sinks of currents, and allows more meaningful interpretation of field potential recordings.

In order to assess the applicability of high-density electrodes for CSD analysis, hippocampal slices were oriented on the 20 × 3 MEA such that the apical CA1 pyramidal dendrites were parallel to the long axis of the array (Figure 6.6A). Monopolar biphasic stimulations were then delivered through one of the electrodes in a peripheral column (in this case, the right column), and evoked responses were recorded on the 59 other electrodes. The left panel in Figure 6.5B shows field potential (FP) activity recorded at the middle column of electrodes in response to a single stimulation in *stratum radiatum* (marked by a red dot). Positive FPs

were observed in *stratum oriens* (above the cell body layer, *stratum pyramidal*), and their reversed negative potentials in *strata radiatum* and *moleculare*. The population spike, seen as a sharp deflection in the waveform, was present on many electrode traces.

The combination of multiple recordings along the pyramidal cell constitutes the FP laminar profile of the CA1 responses. By interpolating the values between adjacent recordings, a topographical map was generated in which voltages were assigned colors. In these color maps, the yellow/red marked the spread of positive EPSPs, and the blue areas delineated negative EPSPs, or the spread of population spikes through positive EPSPs. A CSD of the laminar profile was obtained by applying two-dimensional-CSD analysis to the recorded voltages (Gholmieh G. et al., 2005). The population spike spread was markedly narrower in the 2-D–CSD graphs (right panel, Figure 6.6B). Comparing the FP and CSD (left versus right panel, respectively), color maps showed how CSD also narrowed the longitudinal spread of EPSPs, both the positive and the negative ones. Additionally, CSD analysis unmasked a current source in *stratum moleculare*, which was not visible in the FP. The reversal between the other source and the sink, however, remained at the same location in *stratum pyramidal*.

In summary, spatial activity maps are thus generated by displaying the electrode recording according to their topographical arrangement over the slice. These maps can visualize the spread of a response and the extent of an experimental manipulation's effect. Depending on electrode density, these spatial plots can provide either low resolution information which allows a wide, albeit sparse, coverage of the activity at various slice regions, or at higher density enables CSD analysis for accurate mapping of currents and sources in smaller cellular subregions.

6.2.3 Spatiotemporal Map

The examples above illustrated the power of pMEAs in generating static topographical activity maps by interpolating values between electrodes. The ability to simultaneously record from all electrodes over time, transforms these static maps into dynamic ones that allow visualization of spatiotemporal propagation of activity across a slice.

The propagation of an evoked response from CA3 to CA1 in a hippocampal slice is visualized in Figure 6.7. The mossy fibers of the slice were stimulated by the electrodes marked in red. Each color map illustrates the actual recorded potential at the time point marked in its corner. The sequence of the four frames thus provides a glimpse into the progression of the response over time. A large EPSP is first observed in CA3, as a large negative depolarization color-coded in blue. As the EPSP wanes in CA3, it begins to propagate along the Schaffer collateral fibers towards CA2 and then CA1. From these images, it appears that the deepest depolarization traversed approximately 2 mm in 8 msec, which amounts to 0.25 m/sec. This propagation velocity corresponds to the average value reported for Schaffer collateral fibers by Andersen et al. (2000). The time frames help to visualize easily the propagation of EPSP activity across the slice, which could

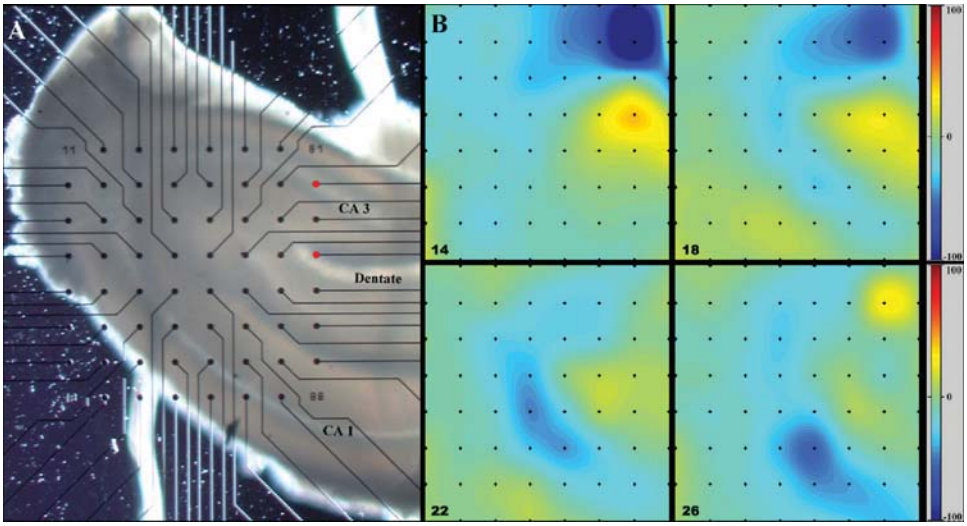

FIGURE 6.7. Propagation of an EPSP along the Schaffer collaterals: (A) photomicrograph of a slice on the pMEA. Red dots mark stimulation site. (B) Four snapshot spatial maps of the recorded potential. The number at the bottom left corner indicates the time elapsed since the stimulation. The pseudo-color range has red at 100 μV and blue at -100 μV.

not be observed at all with single electrode experiments, and would even be hard to discern just by looking at all 60 waveforms.

Although Figure 6.7 traced passive propagation of a postsynaptic potential along the Schaffer collaterals, it is sometimes desirable to trace the activity across synapses in order to see how different subregions are interacting with each other. As part of the biosensor project described in Section 6.2.1, we tested the effects of trimethylolpropane phosphate (TMPP), a byproduct of jet fuel combustion and a $GABA_A$ inhibitor. (Keefer et al., 2001) At 1 mM (Figure 6.8), TMPP disinhibited the slice sufficiently that the monosynaptic population spike in dentate granule cells produced by stimulation in the PP (blue waveforms) was followed by a disynaptic burst of population spikes in CA3. This epileptiform bursting in CA3 slowly spread an EPSP into CA1. Stimulation in CA3 (red waveforms) produced a large monosynaptic population spike in CA3 immediately followed by similar bursting as before and followed by an EPSP in CA1. Finally, stimulation in CA1 (green waveforms) produced a monosynaptic EPSP in CA1 and no activity anywhere else in the slice.

When the responses to the three stimulations were overlaid, propagation across the slice could be clearly visualized by comparing the response delays. The time difference between the first population spike peaks in CA3 triggered by PP and mf stimulations was 12 to 13 msec. These first spikes in CA3 were followed by bursts of spikes 3 to 5 msec apart, and in the case of PP stimulation, the second spike was the largest. The response delay between these two stimulations corresponded

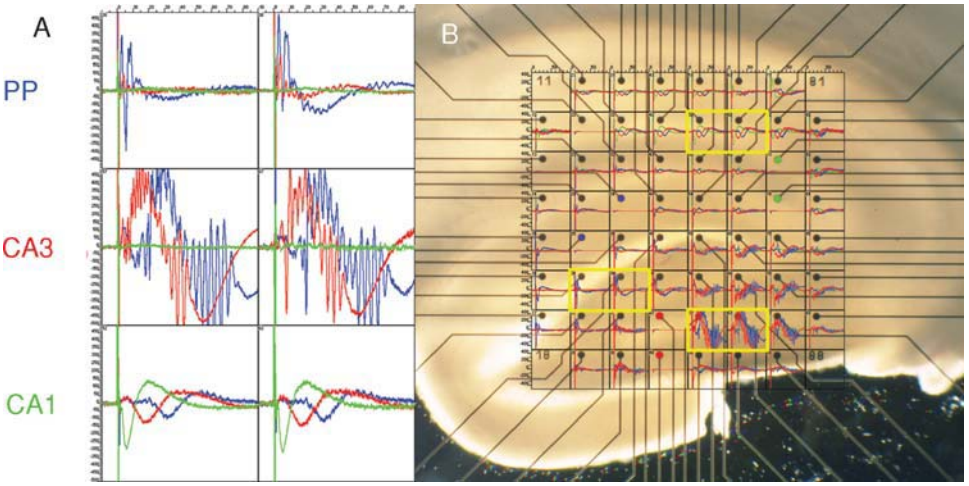

FIGURE 6.8. Effects of 1 mM TMPP application on the hippocampal slice: (A) responses evoked by stimulation at the perforant pathway (PP, blue dots and waveforms), CA3 area (red dots and waveforms), and CA1 (green dots and waveforms); (B) photomicrograph of slice on pMEA overlaid with the responses to the three stimulations. Yellow rectangles show electrodes that are expanded in (A) (*x*-axis 100 msec, *y*-axis 500 μV).

to the EPSP lag observed in CA1 for the same two stimulations (14 msec delay at the troughs). In addition, the EPSP evoked by mf stimulation was delayed 12 msec from the monosynaptic potential elicited by direct stimulation at CA1. These lags reveal that propagation of activity across the slice was facilitated by TMPP. More specifically, TMPP disinhibited the inhibitory neurons in CA3, thus when a sufficient stimulation arrived through the mossy fibers to CA3, the disinhibited pyramidal cells all fired in synchrony (population spike). This population spike spread uninhibited through the recurrent collaterals thereby triggering the observed bursting. All CA3 spikes also traveled along the Schaffer collaterals and produced the observed trisynaptic EPSP in CA1. The delays in CA1 EPSP reflected the number of synapses traversed between the initial stimulation site and the CA1 pyramidal cells. The pMEAs thus enabled not only the localization of the major site of action of TMPP at the CA3 inhibitory interneurons, but also unmasked its facilitatory effect on the propagation of activity throughout the entire trisynaptic pathway of the hippocampal slice.

There appears to be significant variability in the propagation velocity and delays reported in the literature. Using pMEAs, Andersen et al. mapped the angle and distribution of Schaffer collaterals in a sheet-like rat hippocampal preparation, and found a distribution of conduction velocities for different fibers in the hippocampus. They calculated the average conduction velocity of the weakly myelinated Schaffer collateral fibers at 0.25 m/sec, associational fibers averaged 0.39 m/sec, and axons in the fimbria fell into two classes with average velocities of 0.99 and

0.37 m/sec depending on whether they were myelinated (Andersen et al., 2000). Although our results in Figure 6.7 match this value, fibers running parallel to the pyramidal layer were previously reported to have a propagation velocity of 0.3 m/sec in the guinea pig hippocampus. (Andersen et al., 1978) In dissociated hippocampal neuron cultures, conduction velocity was calculated to 0.12 m/sec with multichannel optical recordings with voltage-sensitive dyes, and the synaptic delay was calculated at 1 msec (Kawaguchi et al., 1996).

These differences in velocities are also reflected in the variability of response delays. Our lab has previously reported on trisynaptically evoked population spikes in CA1 from PP stimulations in vivo, where we recorded monosynaptic responses in CA1 at 6 msec, disynaptic ones at 11 msec, and trisynaptic ones at 17 msec, considerably different from the above-reported delays. (Yeckel and Berger, 1995) The monosynaptic and disynaptic responses were postulated to constitute a feedforward circuit, whereby PP feeds directly into CA3 and CA1 (Yeckel and Berger, 1990). Hippocampal trisynaptic response onset delays reported with optical recordings of voltage-sensitive dyes from PP stimulations yielded 5.5 msec delay for granule cells, 6.5 msec for CA3, and 19.2 for CA1. In addition, potentiation by tetanic stimulation decreased the onset latency by 65% at CA1 (Nakagami et al., 1997).

In the isolated guinea pig brain in vitro preparation, Pare and Llinas (1994) measured the population spike latency in CA1 in response to entorhinal cortex (EC) stimulation. They reported spike spatial propagation beyond the transverse axis of the hippocampus, and temporal delays that varied by up to 8 msec depending on the relative recording and stimulation sites. The recorded delays suggested that the topographical relationship between EC and hippocampus, although not spatially confined in lamellae, was preserved in the time domain. They further demonstrated that the spike latency depended on the stimulation intensity, which we also observed in our experiments (data not shown). Furthermore, a 3 msec delay in propagation was observed in CA2 using optical recordings of voltage-sensitive dyes. (Sekino et al., 1997) The transmission from CA3 to CA1 could proceed either directly through the Schaffer collaterals or stop for 3 msec in CA2 before proceeding. The coexistence of these two modes of propagation of activity leads to delays in propagation from CA3 to CA1 that vary from 7 to 6.5 msec. The differences in our reported multisynaptic delays therefore depend on many factors that can be investigated systematically with pMEAs. Of course, higher-density conformal pMEAs could resolve propagation along dendritic trees at higher spatiotemporal resolution, and allow examination of changes of electrical conductance velocity or summation along single cells. In summary, however, the reported propagation velocities and delays point to the power and usefulness of pMEAs for investigations of multisynaptic network activity.

6.2.4 Neuroprosthetic Applications

The pMEAs' ability to stimulate specific regions of a tissue and record its spatiotemporal dynamics makes them useful testbeds for neuroprosthetic devices. We are using our conformal high-density pMEAs to develop a proof-of-concept for a

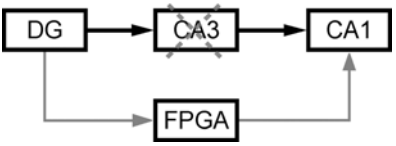

FIGURE 6.9. Diagram of CA3 replacement with a FPGA/VLSI device. The FPGA/VLSI device will replace the functionality of severed CA3, by receiving its inputs and sending out its modeled outputs to CA1.

cortical prosthesis. The goal of this study is to investigate the fundamental science and implement technology that will enable a biomimetic electronic device to be implanted into hippocampus to replace damaged neuronal circuits, and thereby re-establish its original functions. The feasibility of this ambitious endeavor is being first demonstrated in an in vitro hippocampal slice preparation on pMEAs. The proof-of-concept consists of replacing the biological CA3 subregion with an FPGA/VLSI-based model of the nonlinear dynamics of CA3, such that propagation of spatiotemporal patterns of activity in the DG $\rightarrow$ FPGA/VLSI $\rightarrow$ CA1 network reproduces that observed experimentally in the biological DG $\rightarrow$ CA3 $\rightarrow$ CA1 circuit (Figure 6.9) (Berger et al., 2001; Berger et al., 2005).

Inherent to the success of this project is the development of a stable biological preparation that requires optimization of the anatomical and the electrophysiological conditions. Current pMEAs are not optimized for such an application because the symmetrical distribution of electrodes does not match the cytoarchitecture of hippocampal slices (see above). Therefore, we have designed and built a new generation of pMEAs that allow us to record spatiotemporal activity along the trisynaptic pathway of the hippocampal slice. Based on preliminary results obtained with traditional glass electrodes, we mapped the best recording sites from the DG, CA3, and CA1 as shown in Figure 6.10A and used these data to design a new pMEA (Figure 6.9B).

The pMEA designed to replace CA3 included two different circular pad sizes: 28 μm diameter pads that are grouped in series to form sets of stimulating pads in DG (three at a time) and CA1 (two at a time), and 36 μm diameter pads used for recording in DG, CA3, and CA1. By grouping sets of stimulating pads in series, we were able to achieve a significantly larger pad surface area and correspondingly larger total stimulating current than was possible with single pads, while still maintaining essential conformality to cytoarchitecturally relevant features. The first phase of experiments consisted of recording trisynaptic activity in order to build a mathematical model of the CA3 region. Stimulating the perforant pathway fibers, with 5 μM picrotoxin in the aCSF, elicited population spikes in DG and CA3, and an EPSP in CA1 (Figure 6.3C). The delay between population spikes varied from 8 to 10 msec between DG and CA3, and the EPSP in CA1 was similarly delayed from the spike in CA3. Random interval stimulation trains will be sent through the slice to extract the nonlinear dynamics of the circuit as described in Section 6.1.1., and the generated kernels will be implemented in the FPGA.

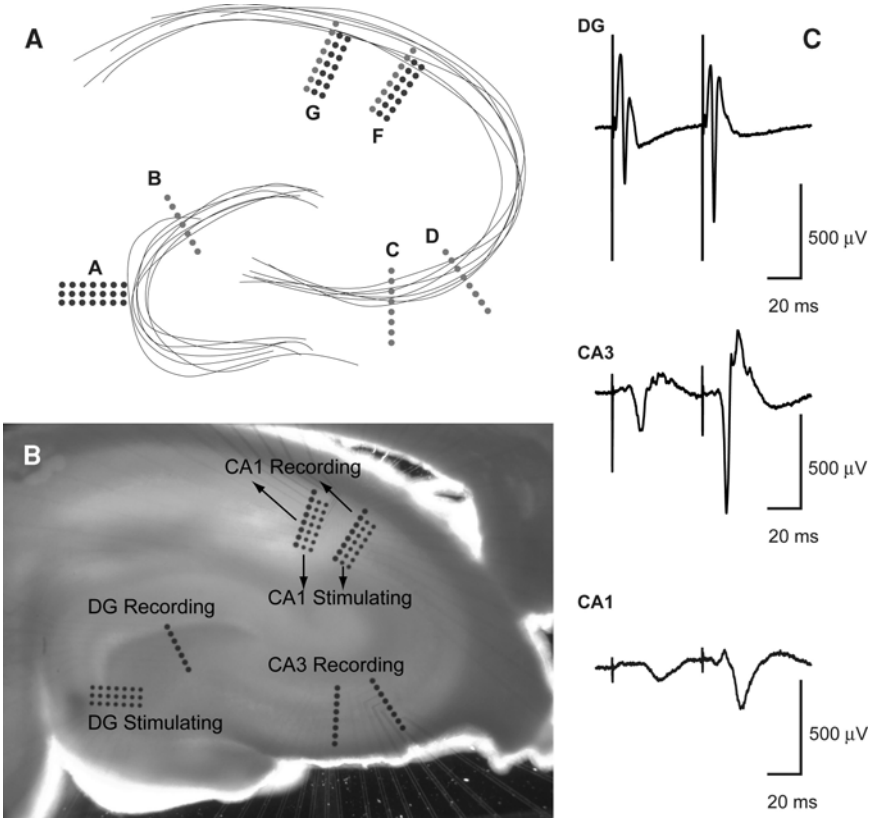

FIGURE 6.10. pMEA for CA3 replacement: (A) the design of conformal multi-electrode array included two different circular pad sizes (A, 3 × 7; F and G, 2 × 7) 28 μm diameter pads with a 50 μm center-to-center spacing grouped in series to form sets of stimulating pads in DG and CA1, and (B, 1 × 7; C, D, F, and G, 1 × 8) 36 μm diameter pads also with a 50 μm center-to-center spacing for recording. The sets are aligned according to rat hippocampal cytoarchitecture covering key input/output regions of DG, CA3, and CA1, thereby allowing complete diagnostic assessment of the nonlinear dynamics of the trisynaptic circuit. (B) Photomicrograph of a slice on the pMEA. (C) Trisynaptic recording from the DG, CA3, and CA1 areas. PP stimulation yielded large populations pikes in DG and CA3 and an EPSP in CA1, all with the appropriate multi-synaptic time delays (scale bars 20 msec and 500 μV).

The second phase of the proof-of-concept involves the severance of CA3–CA1 connections, and replacing the CA3 region dynamics with the FGPA device. The DG responses will then be channeled through the FPGA to the CA1 stimulating electrodes in order to regenerate the biological circuit's output. (Berger et al., 2005) The results from these experiments will allow us to refine our models until we are able to reproduce a CA1 output identical to the one obtained from the intact slice. At that point, we can transfer our acquired knowledge and FPGA to an in

vivo testbed. The pMEA is thus serving as a rapid testing tool for the development of our neuroprosthetic application.

6.3 Discussion

Although sequential single-electrode recordings were used diligently to study network connectivity (Andersen et al., 1971; Yeckel and Berger, 1990, 1995), examining spatiotemporal correlations was not possible with this methodology. Multi-electrode array technology offers several advantages over traditional single-electrode recording in the areas of high-throughput testing, spatial mapping of electrical activity, temporal information processing, spatiotemporal activity monitoring, long-term physiological investigations, and neuroprosthetic-driven network dynamics elucidation. Technological advances have increased the production and use of pMEAs, however, the limited number of electrodes has led to the creation of generic arrays consisting of symmetrical matrices of electrodes that suffer from misalignment with tissue cytoarchitecture due to the nonsymmetrical anatomy of the brain. Elliptic (Thiebaud et al., 1999) or circular (Duport et al., 1999) electrode layouts have been designed for hippocampal slices with a single or double layer of electrodes matching the pyramidal cell layer, however these pMEAs are hard to align to the tissue, and do not record dendritic activity. This chapter introduced four high-density pMEAs that are custom designed for specific in vitro investigations with hippocampal slices. These new arrays are designed for input optimization to area CA1, medial and lateral perforant path differentiation, CSD studies, and recording trisynaptic activity.

In all in vitro electrophysiological experiments, considerable care and time is spent locating appropriate stimulation and recording sites. Herein, the first advantage of pMEAs presents itself for high-throughput experiments, by expediting the process of localizing the optimal stimulation and recording sites in a target area. The first example presented above illustrated the ease with which the optimal recording site or several sites could be selected from a geometrically arranged pMEA. By defining the desired recording criteria, users could quickly select the channels they wished to record and analyze. The redundancy of the channels could serve as a backup for weak signals or damaged electrodes, or to increase the statistical sample size by grouping the recordings into area-specific subsets (e.g., dendritic vs. pyramidal). The second example illustrated how the large number of densely packed electrodes in a conformal array can be used to optimize stimulation and recording sites for finer control over the input–output relation between CA3 and CA1 in the hippocampal slice. One subarray was designed to stimulate the Schaffer collaterals emanating from CA3, and the other subarray recorded activity from the CA1 pyramidal and dendritic areas. By sequentially stimulating pairs of electrodes, we were able to determine the electrode pair that yielded the maximal response, and immediately identify the location of the latter. Across slices, the single peak in the stimulus optimization graph suggested that a narrow bundle of axons was a dominant afferent input, consistently with the Schaffer collateral

fibers being the major excitatory inputs to CA1 (Andersen et al., 1971). Although the sequential approach is reminiscent of microadvancing single electrodes, it is different in that it does not induce incremental damage to the tissue, and in being automatable in software without the need for manual repositioning. Automation of this otherwise tedious input/output optimization process would increase efficiency and productivity in pharmacological drug-screening protocols.

Beyond the gain in speed and efficiency, the ability to stimulate different sites in close proximity to each other without disturbing the tissue by repeated electrode insertions will enable more accurate and concise stimulations. The advantage of such fine spatial control over the stimulation site was illustrated with the selective excitation of PP subpathways. The PP–DG–CA3 high-density pMEA was designed to match the region's anatomy in order to stimulate the two adjacent afferent PP subpathways selectively and differentiate between their responses. The design is intended to study the subpathway's differential effects on the CA3 output response; however, for this experiment we focused just on the DG's granule cell's postsynaptic potentials in order to illustrate the pMEA's ability to selectively target each subdivision.

Although the subdivisions can be experimentally distinguished by their responses to pp stimulation, electrophysiological studies often do not specify which of the subdivisions is being stimulated due to the difficulty in selectively targeting them. This pathway differentiation was easily achieved with this pMEA (Figure 6.4), where stimulating the lateral PP with one pair of electrodes exhibited pp facilitation mostly in the lateral molecular layer, whereas stimulating the medial PP produced pp depression in the medial molecular layer, which reversed into current sources in the lateral molecular layer. These responses were consistent with the electrode's anatomical location. This experiment demonstrated the advantage of high-density pMEAs in effortlessly stimulating specific brain subdivisions and distinguishing their responses in the same slice. The versatility of custom designing such high-density pMEAs will enable and speed up new electrophysiological experiments in various tissues where there is a need for selective stimulation of adjacent pathways. Research on brain slices with sharp cytoarchitectural boundaries such as the rat barrel cortex (Wirth and Luscher, 2004), or defined fiber tracts such as the cerebellum (Heck, 1995, Egert et al., 2002), would benefit significantly from high-density pMEAs that conform to their geometries.

pMEAs are, however, more than just a sum of many electrodes that allow rapid accumulation of many channels of electrophysiological data from a single slice. pMEAs allow the creation of spatiotemporal activity maps that enable many new applications not previously possible with single-electrode recordings. Spatially, activity maps allow tracing of the spread of a response across a tissue. Figure 6.5 illustrated how this information can be useful in an LTP experiment in the hippocampal slice. We can trace the area responding to a stimulation by color-mapping the EPSP amplitude on the slice image (A,B), and we can similarly map out the amount of potentiation (C) in order to visually determine the extent and spread of these parameters over the entire slice. Mapping various activity parameters spatially onto the slice is especially useful for studying topographically

organized brain structures such as cortical areas (visual, auditory, barrel, etc.), which have functionally distinct subdivisions.

Information about the activity in different cellular layers (*strata*) can only be mapped with higher-density arrays that sample closely enough to enable CSD analysis. This mathematical transformation is necessary to compensate for the field potentials intermixing in conductive tissue, and to resolve current sources and sinks. The electrode spacing requirement depends on the distance from the source and the size of different spatial domains in the slice, and as such has been estimated at 50 μm (Novak and Wheeler, 1989). Our high-density pMEAs have electrodes spaced 50 μm apart (center to center) specifically for this purpose. Figure 6.6 illustrated the ability of CSD analysis to reduce the spatial spread of field potentials and accurately localize current sources and sinks and even unmask some that may be overpowered by larger potentials. CSD analysis produced a more accurate laminar profile of the CA1 pyramidal cell EPSP and population spike. The CSD profiles could thus be used to map activity along axo-dendritic trees that densely orient parallel to each other. Kim et al. (submitted) used our rectangular high-density pMEA to localize estradiol's effect on CA3 pyramidal cells and compare the activity maps to the distribution of estrogen receptors. High-density pMEAs can thus be used for generating accurate high-resolution spatial activity maps of a tissue, thereby complementing larger-scale maps generated by more widely spaced pMEAs.

There are many applications to purely temporal or long-term recordings from pMEAs as illustrated in Chapters 16 and 17 of this book, which investigate circadian rhythmicity and slice cultures, or the temporal dynamic investigations of Beggs et al. (2003) and Jimbo et al. (1999). However, we did not present examples of such approaches here, as our high-density conformal pMEAs do not confer any significant advantages for solely temporal experiments, and in the case of long-term cultures, the tissue changes its position relative to the electrodes during the span of the culture in ways that are not controllable, and thus makes conformal pMEA design obsolete. On the other hand, in Chapter 7, the authors presented methods of patterning adhesion molecules onto arrays in order to control the development of networks according to set geometries. These patterned networks can be aligned to electrode locations and thereby allow long-term monitoring and investigations of their activity.

Spatiotemporal information is, however, the most distinguishing advantage of MEAs, as they permit the simultaneous recording of activity at many points across a tissue, thereby revealing correlations and interactions between different regions. The activity in a slice spreads from one area to another along excitatory pathways. This propagation can be traced in space over time with pMEAs. We traced the EPSP produced by Schaffer collateral activation at CA3. First, cells in CA3 itself responded through recurrent afferents, the response then propagated to CA2 pyramidal cells, and proceeded to CA1. A movie of the activity could be generated by color-coding the potentials and interpolating between them at every time frame. Four frames of such a movie are shown in Figure 6.7 to illustrate the spread of the activity across the slice over time.

The interaction between hippocampal areas was more specifically explored in our TMPP investigations. TMPP, a $GABA_A$ inhibitor, reduces inhibition in hippocampal slices. In CA3, large number of inhibitory interneurons usually prevents repetitive bursting due to activation of recurrent fibers. In the presence of TMPP, this inhibition was blocked, and CA3 pyramidal cells would burst synchronously when stimulated either directly or upstream, through PP stimulation. The burst of population spikes was easily localized to area CA3 by the pMEA. A facilitated propagation of the response to CA1 was also observed, and the delay in CA1 EPSP indicated the number of synapses traversed by the spreading activity. Monosynaptic responses could be easily compared to di- and trisynaptic ones by overlaying recorded potentials and comparing lag times. The effect of TMPP on the hippocampal slice was thus more than just disinhibiting CA3 pyramidal cells to the point of evoking epileptiform activity: it also facilitated propagation of this activity to CA1. This network effect of TMPP on the hippocampal slice could not have been observed with single-electrode intracellular recordings, although the latter revealed epileptiform discharges in CA1 that we did not detect extracellularly (Lin et al., 2001). MEAs are therefore extremely useful for investigating the propagation of epileptiform activity in vivo and in vitro, spontaneous or drug-induced (Nagao et al., 1996; Harris and Stewart, 2001). pMEAs have been used to localize the origin of epileptic seizures (optical multi-site recordings; Colom and Saggau, 1994), to determine the propagation direction (Harris and Stewart, 2001), and calculate changes in propagation velocity across fibers compared to normal states (Holsheimer and Lopes da Silva, 1989). Beyond drug screening, such monitoring of multi-synaptic activity in a tissue is thus useful for investigations of network connections and dynamics in normal or diseased states. In these investigations, observing the entire slice with pMEAs not only allows localization of the site of activity of the drug, but can also unveil related effects on other areas.

pMEAs have been used for time spreading activity or trace waves in several tissue preparations: retina (Syed et al., 2004), cerebellum (Egert et al., 2002), barrel cortex (Wirth and Luscher, 2004), and so on. pMEAs allow easy quantification of propagation velocity across a slice. In our first activity propagation example, the monosynaptic response spread along the Schaffer collaterals at 0.25 m/sec was consistent with the 0.25 m/sec reported average velocity for this weakly myelinated fiber (Andersen et al., 2000). There are, however, many other measurements of axonal propagation speed that show different values, and our synaptic delay times calculated from the TMPP experiment appear longer than those reported in the literature. The speed of propagation of activity in a tissue preparation is generally thought of as a function of the axon thickness, their myelination, length, and also the number of traversed synapses. There are, however, numerous other factors that can influence the propagation velocity across the multi-synaptic pathways, beyond simple experimental manipulations such as temperature or ionic concentration differences (our unpublished data). In particular for hippocampus, the behavioral state (REM, slow-wave sleep, or alert; Winson and Abzug, 1978) irregular or theta EEG (Herreras et al., 1987), anesthesia (Buzsaki et al., 1986; Pare and Llinas, 1994), pharmacological disinhibition or activation facilitation (Sirvio et al., 1996),

stimulation frequency (Herreras et al., 1987; Yeckel and Berger, 1990), stimulation intensity and relative location to recording sites (Pare and Llinas, 1994; our unpublished observations), and animal species (Andersen et al., 1978) have all been shown to affect activity propagation in the trisynpatic pathway. pMEAs are extremely well suited for investigating these variables to elucidate the interrelations between connected regions in multi-synaptic circuits.

Such an understanding of network dynamics is critical for building biomimetic devices or neuroprosthetics. The retinal prosthesis project relies on pMEA recordings from in vitro retinal preparations to develop stimulation algorithms for its implanted MEAs (Meister et al., 1994; Warland et al., 1997; Chichilnisky and Kalmar, 2003; Humayun et al., 2003; Frechette et al., 2004). In our project to replace the CA3 function in vivo, we needed an in vitro model upon which to test our nonlinear mathematical models of the input–output properties CA3. The first step entailed development of a slice-pMEA preparation that allows experimental characterization of the combined nonlinear dynamics of the intrinsic hippocampal trisynaptic circuit. The conformality aspect of the newly designed pMEA was crucial to obtain trisynaptic recordings from hippocampal slices because it is extremely difficult if not impossible to obtain simultaneous dentritic and somatic responses in the three subregions of the hippocampus using the commercially available MEAs with their sparse and symmetrical matrices of electrodes. The novel pMEA has recording electrodes in the DG, CA3, and CA1 regions as well as stimulating electrodes in the DG and the CA1 regions. The DG stimulating electrodes were used to activate the perforant path, and the CA1 stimulating electrodes were used to channel the FPGA/VLSI output to the CA1 pyramidal cells.

Using the designed pMEA, we have recorded trisynaptic responses in the disinhibited hippocampal slice in response to PP stimulation trains consisting of 2000 electrical pulses with Poisson-distributed random intervals. We recorded population spikes in DG and CA3 and dentritic EPSPs in CA1, with delays comparable to those obtained under TMPP disinhibition, but without the CA3 epileptiform activity. The population spike amplitude was extracted to build a nonlinear mathematical model of CA3 (Gholmieh et al., 2004b) that is now implemented in hardware using an FPGA device (Granacki et al., 2004). Currently, we are exploring the next stage of the project, which involves replacing CA3 with a FPGA. First we cut the Schaffer collaterals, and then we send the DG's responses into the FPGA and redirect the FPGA's output (CA3 replacement) to the CA1 stimulating electrodes. We then record the corresponding CA1-evoked responses and compare them to those obtained from intact slices. Our preliminary results indicate that our VLSI model is succeeding at replacing the severed CA3 area (Gholmieh et al., 2004b). This in vitro slice preparation on conformal pMEA approach is allowing us to test several computational and analytical parameters rapidly before any implantation into live animals. Once the FPGA/VLSI model is fine tuned and accurately reproduces CA1 output comparable to the intact, we will connect it to MEAs implanted in rat hippocampus, and repeat the same experiments. Our pMEA work would have thus expedited the development process, from the generation of the nonlinear

model to its VLSI testing, and thereby also minimized animal use (because we obtain several hippocampal slices from each rat brain).

In summary, rapid transition of cell types in the brain mandates high spatial resolution sampling whereas the nonsymmetrical organization of the brain in conjuction with the limited number of recording channels requires conformal electrode designs. In this chapter, four pMEAs were introduced that illustrated the advantages of the conformality and high density for in vitro electrophysiological experiments with acute hippocampal slices. The high-density conformal designs confer new abilities to the planar MEA research tool whether it is applied to rapidly and accurately localize target field responses, to increase sampling sites for high-throughput drug investigations, or to trace spatiotemporal network activity propagation and dynamics for biomimetic neuroprosthetic applications. The work presented here lays the ground for the custom design of conformal high-density pMEAs that meet the individual needs of their application.

References

Andersen, P., Bliss, T.V.P., and Skrede, K.K. (1971). Lamellar organization of hippocampal excitatory pathways. *Exper. Brain Res.* 13: 222–238.

Andersen, P., Silfvenius, H., Sundberg, S.H., Sveen, O., and Wigstrom, H. (1978). Functional characteristics of unmyelinated fibres in the hippocampal cortex. *Brain Res*. 144(1): 11–18.

Andersen, P., Soleng, A.F., and Raastad, M. (2000). The hippocampal lamella hypothesis revisited. *Brain Res*. 886(1–2): 165–171.

Beggs, J.M. and Plenz, D. (2003). Neuronal avalanches in neocortical circuits. *J. Neurosci*. 23(35): 11167–11177.

Berger, T.W., Ahuja, A., Courellis, S.H., Erinjippurath, G., Gholmieh, G., Granacki, J.J., Marmarelis, V.Z., Srinivasan, V., Dong, S., Tanguay, A.R., and Wills, J. (2005). Brain-implantable biomimetic electronics as neural prostheses to restore lost cognitive function. Towards Replacement Parts for the Brain: Implantable Biomimetic Electronics as Neural Prostheses. Eds. Berger, T.W. and Glanzman, D.L. MIT Press, Cambridge MA.

Berger, T.W., Baudry, M., Brinton, R.D., Liaw, J.S., Marmarelis, V.Z., Park, AY., Sheu B.J., and Tanguay, A.R.J. (2001). Brain-implantable biomimetic electronics as the next era *Neural Prosthet. Proc. IEEE* 89(7): 993–1012.

Buzsaki, G., Czopf, J., Kondakor, I., and Kellenyi, L. (1986). Laminar distribution of hippocampal rhythmic slow activity (RSA) in the behaving rat: Current-source density analysis, effects of urethane and atropine. *Brain Res*. 365(1): 125–137.

Chapin, J.K., Moxon, K. A., Markowitz, R.S., and Nicolelis, M.A. (1999). Real-time control of a robot arm using simultaneously recorded neurons in the motor cortex. *Nat. Neurosci*. 2(7): 664–670.

Chichilnisky, E.J. and Kalmar, R.S. (2003). Temporal resolution of ensemble visual motion signals in primate retina. *J. Neurosci.* 23(17): 6681–6689.

Colom, L.V. and Saggau, P. (1994). Spontaneous interictal-like activity originates in multiple areas of the CA2–CA3 region of hippocampal slices. *J. Neurophysiol.* 71(4): 1574–1585.

Dahl, D., Burgard, E.C., and Sarvey, J.M. (1990). NMDA receptor antagonists reduce medial, but not lateral, perforant path-evoked EPSPs in dentate gyrus of rat hippocampal slice. *Exp. Brain Res*. 83(1): 172–177.

Duport, S., Millerin, C., Muller, D., and Correges, P. (1999). A metallic multisite recording system designed for continuous long-term monitoring of electrophysiological activity in slice cultures. *Biosens. Bioelectron*. 14(4): 369–376.

Egert, U., Heck, D., and Aertsen, A. (2002). Two-dimensional monitoring of spiking networks in acute brain slices. *Exp. Brain Res.* 142(2): 268–274.

Frechette, E.S., Sher, A., Grivich, M.I., Petrusca, D., Litke, A.M., and Chichilnisky, E.J. (2005). Fidelity of the ensemble code for visual motion in primate retina. *J. Neurophysiol.* 94: 119–135.

Gholmieh, G., Courellis, S., Dimoka, A., Wills, J.D., LaCoss, J., Granacki, J.J., Marmarelis, V., and Berger, T.W. (2004a). An algorithm for real-time extraction of population EPSP and population spike amplitudes from hippocampal field potential recordings. *J. Neurosci. Meth.*136(2): 111–121.

Gholmieh, G., Courellis, S., Fakheri, S., Cheung, E., Marmarelis, V., Baudry, M., and Berger, T.W. (2003). Detection and classification of neurotoxins using a novel short-term plasticity quantification method. *Biosens. Bioelectron.* 18(12): 1467–1478.

Gholmieh, G., Courellis, S.H., Hsiao, M., Srinivasan, V., Ahuja, A.K., LaCoss, J., Wills, J.D., Tanguay, A.R., Jr., Granacki, J.J., and Berger, T.W. (2004b). A biomimetic electronic prosthetic for hippocampus: Proof-of-concept using the *in vitro* slice. *Soc. Neurosci*. Online Abstract Viewer.

Gholmieh, G., Soussou, W., Courellis, S., Marmarelis, V.Z., Berger, T.W., and Baudry, M. (2001). A biosensor for detecting changes in cognitive processing based on nonlinear systems analysis. *Biosens.Bioelectron.*16(7–8): 491–501.

Gholmieh, G., Soussou, W., Han, M., Ahuja, A., Hsiao, M.-C., Dong, S., Tanguay, A.R. Jr., and Berger, T.W. (2005). Custom-designed high-density conformal planar multielectrode arrays for brain slice electrophysiology. *J Neurosci Meth*. 10.1016.

Granacki, J.J., Wills, J.D., LaCoss, J., Courellis, S.H., Marmarelis, V.Z., Gholmieh, G., and Berger, T.W. (2004). A biomimetic electronic prosthetic for hippocampus: hardware model of CA3 nonlinear dynamics, *Soci. Neurosci*. Online Abstract Viewer.

Gross, G.W. and Schwalm, F.U. (1994). A closed flow chamber for long-term multichannel recording and optical monitoring. *J. Neurosci. Meth.* 52(1): 73–85.

Gross, G.W., Keefer, E.W., Pancrazio, J.J., and Stenger, D.A. (1999). Rapid determination of toxic effects of trimethylol propane phosphate usina neuronal networks on microelectrode arrays. *Soc. Neurosci. Abstr*. 1(230.13).

Gross, G.W., Rhoades, B.K., Azzazy, H.M., and Wu, M.C. (1995). The use of neuronal networks on multielectrode arrays as biosensors. *Biosens. Bioelectron*. 10(6–7): 553–567.

Harris, E. and Stewart, M. (2001). Propagation of synchronous epileptiform events from subiculum backward into area CA1 of rat brain slices. *Brain Res*. 895(1–2): 41–49.

Heck, D. (1995). Investigating dynamic aspects of brain function in slice preparations: spatiotemporal stimulus patterns generated with an easy-to-build multi-electrode array. *J. Neurosci. Meth*. 58(1–2): 81–87.

Herreras, O., Solis, J.M., Martin del Rio, R., and Lerma, J. (1987). Characteristics of CA1 activation through the hippocampal trisynaptic pathway in the unanaesthetized rat. *Brain Res*. 413(1): 75–86.

Holsheimer, J. and Lopes da Silva, F.H. (1989). Propagation velocity of epileptiform activity in the hippocampus. *Exp. Brain Res.* 77(1): 69–78.

Humayun, M.S., Weiland, J.D., Fujii, G.Y., Greenberg, R., Williamson, R., Little, J., Mech, B., Cimmarusti, V., Van Boemel, G., Dagnelie, G., and de Juan, E. (2003). Visual

perception in a blind subject with a chronic microelectronic retinal prosthesis. *Vis. Res*. 43(24): 2573–2581.

Ishizuka, N., Cowan, W.M., and Amaral, D.G. (1995). A quantitative analysis of the dendritic organization of pyramidal cells in the rat hippocampus. *J. Comp. Neurol.* 362(1): 17–45.

Jahnsen, H., Kristensen, B.W., Thiebaud, P., Noraberg, J., Jakobsen, B., Bove, M., Martinoia, S., Koudelka-Hep, M., Grattarola, M., and Zimmer, J. (1999). Coupling of organotypic brain slice cultures to silicon-based arrays of electrodes. *Methods* 18(2): 160–172.

Jimbo, Y. and Robinson, H.P. (2000). Propagation of spontaneous synchronized activity in cortical slice cultures recorded by planar electrode arrays. *Bioelectrochem*. 51(2): 107–115.

Jimbo, Y., Tateno, T., and Robinson, H.P. (1999). Simultaneous induction of pathway-specific potentiation and depression in networks of cortical neurons. *Biophys. J*. 76(2): 670–678.

Kawaguchi, H., Tokioka, R., Murai, N., and Fukunishi, K. (1996). Multichannel optical recording of neuronal network activity and synaptic potentiation in dissociated cultures from rat hippocampus. *Neurosci. Lett.* 205(3): 177–180.

Keefer, E.W., Gramowski, A., Stenger, D.A., Pancrazio, J.J., and Gross, G.W. (2001). Characterization of acute neurotoxic effects of trimethylolpropane phosphate via neuronal network biosensors. *Biosens. Bioelectron.* 16(7–8): 513–525.

Kim, M.T., Gholmieh, G., Soussou, W., Ahuja, A., Tanguay, Jr., A.R., Berger, T.W., and Brinton, R.D. (submitted). 17-beta estradiol potentiates fEPSP within each subfield of the hippocampus with greatest potentiation of the associational/commissural afferents of CA3.

Lin, J., Ritchie, G.D., Stenger, D.A., Nordholm, A.F., Pancrazio, J.J., and Rossi, J., 3rd (2001). Trimethylolpropane phosphate induces epileptiform discharges in the CA1 region of the rat hippocampus. *Toxicol. Appl. Pharmacol.* 171(2): 126–134.

McNaughton, N. and Miller, J.J. (1984). Medial septal projections to the dentate gyrus of the rat: electrophysiological analysis of distribution and plasticity. *Exp. Brain Res.* 56(2): 243–56.

Meister, M., Pine, J., and Baylor, D.A. (1994). Multi-neuronal signals from the retina: acquisition and analysis. *J. Neurosci. Meth.* 51(1): 95–106.

Miyakawa, H. and Kato, H. (1986). Active properties of dendritic membrane examined by current source density analysis in hippocampal CA1 pyramidal neurons. *Brain Res*. 399(2): 303–309.

Morin, F.O., Takamura, Y., and Tamiya E. (2005). Investigating neuronal activity with planar microelectrode arrays: achievements and new perspectives. *J Biosci Bioeng*. 100(2): 131–143.

Nagao, T., Alonso, A., and Avoli, M. (1996). Epileptiform activity induced by pilocarpine in the rat hippocampal-entorhinal slice preparation. *Neuroscience* 72(2): 399–408.

Nakagami, Y., Saito, H., and Matsuki, N. (1997). Optical recording of trisynaptic pathway in rat hippocampal slices with a voltage-sensitive dye. *Neuroscience* 81(1): 1–8.

Nicholson, C. and Freeman, J.A. (1975). Theory of current source-density analysis and determination of conductivity tensor for anuran cerebellum. *J. Neurophysiol.* 38(2): 356–368.

Novak, J.L. and Wheeler, B.C. (1989). Two-dimensional current source density analysis of propagation delays for components of epileptiform bursts in rat hippocampal slices. *Brain Res.* 497(2): 223–230.

Pare, D. and Llinas, R. (1994). Non-lamellar propagation of entorhinal influences in the hippocampal formation: multiple electrode recordings in the isolated guinea pig brain in vitro. *Hippocampus* 4(4): 403–409.

Pine, J. (1980). Recording action potentials from cultured neurons with extracellular microcircuit electrodes. *J. Neurosci. Meth*. 2(1): 19–31.

Sekino, Y., Obata, K., Tanifuji, M., Mizuno, M., and Murayama, J. (1997). Delayed signal propagation via CA2 in rat hippocampal slices revealed by optical recording. *J. Neurophysiol*. 78(3): 1662–1668.

Shimono, K., Baudry, M., Panchenko, V., and Taketani, M. (2002). Chronic multichannel recordings from organotypic hippocampal slice cultures: Protection from excitotoxic effects of NMDA by non-competitive NMDA antagonists. *J. Neurosci. Meth*. 120(2): 193–202.

Shimono, K., Brucher, F., Granger, R., Lynch, G., and Taketani, M. (2000). Origins and distribution of cholinergically induced beta rhythms in hippocampal slices. *J. Neurosci.* 20(22): 8462–8473.

Singer, W. (2000). Why use more than one electrode at a time? *New Technol. Life Sci: Trends Guide* 2000: 12–17.

Sirvio, J., Larson, J., Quach, C.N., Rogers, G.A., and Lynch, G. (1996). Effects of pharmacologically facilitating glutamatergic transmission in the trisynaptic intrahippocampal circuit. *Neuroscience* 74(4): 1025–1035.

Steward, O. (1976). Topographic organization of the projections from the entorhinal area to the hippocampal formation of the rat. *J. Comp. Neurol.* 167(3): 285–314.

Stoppini, L., Duport, S., and Correges, P. (1997). A new extracellular multirecording system for electrophysiological studies: Application to hippocampal organotypic cultures. *J. Neurosci. Meth*. 72(1): 23–33.

Syed, M.M., Lee, S., He, S., and Zhou, Z.J. (2004). Spontaneous waves in the ventricular zone of developing mammalian retina. *J. Neurophysiol*. 91(5): 1999–2009.

Thiebaud, P., Beuret, C., Koudelka-Hep, M., Bove, M., Martinoia, S., Grattarola, M., Jahnsen, H., Rebaudo, R., Balestrino, M., Zimmer, J., and Dupont, Y. (1999). An array of Pt-tip microelectrodes for extracellular monitoring of activity of brain slices. *Biosens. Bioelectron.* 14(1): 61–5.

Thiebaud, P., de Rooij, N.F., Koudelka-Hep, M., and Stoppini, L. (1997). Microelectrode arrays for electrophysiological monitoring of hippocampal organotypic slice cultures. *IEEE Trans. Biomed. Eng.* 44(11): 1159–63.

Warland, D.K., Reinagel, P., and Meister, M. (1997). Decoding visual information from a population of retinal ganglion cells. *J. Neurophysiol*. 78(5): 2336–2350.

Wheeler, B.C. and Novak, J.L. (1986). Current source density estimation using microelectrode array data from the hippocampal slice preparation. *IEEE Trans. Biomed. Eng.* 33(12): 1204–1212.

Winson, J. and Abzug, C. (1978). Dependence upon behavior of neuronal transmission from perforant pathway through entorhinal cortex. *Brain Res.* 147(2): 422–427.

Wirth, C. and Luscher, H.R. (2004). Spatiotemporal evolution of excitation and inhibition in the rat barrel cortex investigated with multielectrode arrays. *J. Neurophysiol.* 91(4): 1635–1647.

Yeckel, M.F. and. Berger, T.W. (1990). Feedforward excitation of the hippocampus by afferents from the entorhinal cortex: Redefinition of the role of the trisynaptic pathway. *Proc. Natl. Acad. Sci.* 87: 5832–5836.

Yeckel, M.F. and Berger, T.W. (1995). Monosynaptic excitation of hippocampal CA1 pyramidal cells by afferents from the entorhinal cortex. *Hippocampus* 5(2): 108–114.